Materials Advances

ROYAL SOCIETY OF CHEMISTRY

PAPER

View Article Online
View Journal | View Issue

Cite this: *Mater. Adv.*, 2025, 6, 3678

Onsite naked-eye detection and quantification of Cu(II) ions in drinking water using N-doped carbon nanodots†

Nidhisha V. and Renuka Neeroli Kizhakayil *

Carbon nanodots (CNDs), benefitted by an array of fine features, have emerged as exemplary members among the various carbon forms in the nanoregime. This study unveils the potential of N-doped CNDs for visual detection and quantification of trace Cu(II) ions in water. Green synthesis was adopted, and the system was characterised using Transmission Electron Microscopy (TEM), X-ray diffraction (XRD), X-ray photoelectron spectroscopy (XPS) Raman spectroscopy, Fourier transform infrared (FT-IR), UV-visible absorbance, and fluorimetric spectral analysis. Dual-emissive CNDs of average size of 2.8 nm with an N-doped carbon core and associated carboxyl, amino, hydroxyl, and carbonyl functional groups were identified. Naked-eye detection of Cu(II) ions was effortlessly achieved, as evidenced by a distinct colour change in the solution, with a lower limit of detection of 20 μM, which is a highly significant value in the context of the permissible amount of copper in drinking water. Further, lower detection was achieved *via* fluorimetric sensing. The detection method was also successfully extended to a solid-state sensor strip, which is desirable for practical onsite applications. An in-depth analysis supported by microscopic and spectral characterisation supported the formation of copper hydroxynitrate as the basis of the detection strategy.

Received 25th January 2025,
Accepted 4th April 2025

DOI: 10.1039/d5ma00068h

rsc.li/materials-advances

Introduction

Copper ions, the third most abundant transition metal ions in the human body, have attracted much attention from the researchers owing to their pivotal role in diverse biological processes. Copper ions are indispensable for the production of essential compounds such as haemoglobin, myelin, and melanin and play a vital role in the normal functioning of the thyroid gland. Copper ions are integral to diverse biological systems, influencing the structural and catalytic properties of significant enzymes and contributing to overall physiological well-being.[1–7] However, maintaining a delicate balance of the species in the body is of principal significance, as both copper deficiency and excess are associated with various disorders, which mandates precise determination of this analyte. Some of the established techniques for this purpose are inductively coupled plasma mass spectrometry,[8–10] high-performance liquid chromatography, atomic absorption spectrometry,[11] atomic fluorescence spectroscopy,[12] and graphite furnace atomic absorption spectroscopy.[13] However, the development of simpler yet effective detection methods is particularly crucial for instantaneous and interference-free on-site identification of the analyte. There exist several metal–organic frameworks for the detection of metal ions.[14–16] Recent reviews have highlighted various optical methods that are effective for cupric ion sensing.[17,18]

In recent years, various carbon nanomaterials have emerged as promising sensing platforms for the detection of metal ions, including copper.[19] Carbon nanotubes, graphene and graphene oxide have been explored for their potential in sensing copper ions.[20–22] In this study, carbon nanodots (CNDs) are presented as an elegant optical sensor to detect Cu^{2+} in aqueous media. CNDs, functionalised graphitic particles < 10 nm in size, feature inherent luminescence, biocompatibility, aqueous dispersibility, and photostability. Their luminescent property makes them covetable candidates for sensing an array of analytes. Heavy metal ion sensing using carbon nanodots has been the subject of extensive investigations.[23–27] Carbon nanodots are widely used for the fluorimetric sensing of Cu^{2+}, taking advantage of the turn-on and turn-off mechanisms in fluorescence[28–30] and colourimetric approaches.[31–33] Herein, *p*-phenylenediamine-derived N-doped CNDs (PD-CNDs) enable trace level detection and quantification of Cu^{2+} ions in drinking water, where the permissible amount of this analyte ion is 31.5 μM, as per the World Health Organization (WHO). PD-CND-mediated distinct colour change enables naked-eye detection of Cu^{2+} even at 20 μM level, a concentration well

Advanced Materials Research Centre, Department of Chemistry, University of Calicut, Kerala 673635, India. E-mail: renuka@uoc.ac.in

† Electronic supplementary information (ESI) available: Optical features of PD-CNDs, real sample analysis results, reproducibility experiment, and elemental mapping of complex. See DOI: https://doi.org/10.1039/d5ma00068h

below the permissible amount. The approach is further extended to develop solid-state sensor strips that are desirable for onsite applications. Excellent selectivity of the system among the metal ions tested in both solution and solid phases demonstrates the merit of the system. The fluorimetric technique allows the quantification of cupric ions down to 2.28 μM. The sensing mechanism was probed in detail using various analytical tools, and identified a sensing strategy operating through the formation of a basic salt of copper, copper hydroxynitrate.

Experimental

Materials

p-Phenylenediamine (PD) was purchased from TCI Chemicals (India) Pvt. Ltd. Chloride or nitrate salts of metal ions (Fe^{3+}, Mg^{2+}, Ba^{2+}, Ca^{2+}, Pb^{2+}, Cr^{2+}, and K^{+}) were purchased from Sisco Research Laboratories Pvt. Ltd, India. Nitrates of Cu^{2+}, Zn^{2+} and Cd^{2+} and $MnCl_2$ were purchased from Alfa Aesar. Nickel nitrate and mercuric chloride were purchased from Hi Media Laboratories Pvt. Ltd, India. Sodium chloride was purchased from Qualigens. All commercially available reagent-grade chemicals were used as received without further purification. Deionized (DI) water was used in all of the reported experiments.

Characterizations

The comprehensive characterization approach provides information about the structural, morphological and optical properties of carbon nanodots, for which high-resolution TEM, XRD, XPS, Raman spectroscopy, FT-IR, UV-vis absorbance and fluorescence spectroscopy techniques were used. The morphology and particle size of the CNDs were determined using a JEOL JEM 2100 high-resolution TEM instrument operating at an accelerating voltage of 200 kV. A Rigaku Miniflex-II diffractometer was used to record the XRD pattern of the sample in the scan range of 2θ 10–90° with Cu Kα radiation. The Raman spectra were obtained using a WITec alpha300RRA (WITec GmbH, Ulm, Germany) with a 532 nm laser. The surface element composition was obtained through XPS spectroscopy and was collected using an Omicron spectrometer using 1253 eV Mg K_α radiation. The FT-IR spectrum was recorded using a JASCO FTIR-4100 spectrometer *via* the KBr pellet method. UV-vis absorption spectra were recorded with the help of a JASCO V-550 spectrometer. A Cary Eclipse fluorescence spectrometer (Agilent technology) was used to obtain the fluorescence spectra. Fluorescence lifetime studies were conducted using a HORIBA-time-correlated single photon counting (TCSPC) system with 370 nm Nano LED as the excitation source. An LZC-4X photoreactor was used to monitor the luminescent features of the systems under UV illumination. The photostability of the materials was assessed using an LZC-4X photoreactor.

Preparation of PD-CNDs

Typically, 0.05 g of *p*-phenylenediamine was dissolved in 60 mL of deionized water. The solution was sonicated for 10 min, transferred into a Teflon-lined autoclave, and subjected to hydrothermal treatment. Different reaction temperatures (120, 150, 180 and 200 °C) and durations (2, 5, 8 and 10 hours) have been tried for the synthesis. The optimal conditions for maximum intensity of CNDs were selected to be 180 °C and 8 h. After cooling, the aqueous solution was centrifuged at 3000 rpm for 30 min, followed by filtration and dialysis. The fractions with significant luminescence were collected and used for further characterization and applications. The normal pH of the solution (pH ∼ 7) was used in the studies because the maximum luminescence was noted at neutral pH.

Visual detection of Cu^{2+} ions using PD-CNDs

All the measurements for Cu(II) ion determination were performed against a reference (blank) solution prepared by adding 1 mL of DI water to 1 mL of PD-CND sensing solution and gently shaking the mixture for 15 s. A typical experiment in the presence of selected metal ions was performed by adding 1 mL of the specific metal ion salt solution in DI water (1 mM) to 1 mL of the PD-CND sensing solution and gently shaking the mixture for 15 s. The experiments were repeated using drinking water collected locally from the University of Calicut campus to confirm the validity of the system.

Quantification of Cu(II) ions using fluorimetry

A stock solution of 15 selected metal ions was prepared in DI water. 300 μL of PD-CNDs solution in 2 mL of DI water was placed in a cuvette. Analyte solutions of specified concentrations were added, and the response was monitored using fluorescence spectroscopy at an excitation wavelength of 440 nm.

Results and discussion

Characterization of the PD-CNDs

The TEM image of the PD-CNDs presented in Fig. 1a shows spherical particles of <10 nm in size. The average particle size determined using the TEM image was 2.8 nm, which was evident from the distribution histogram shown in Fig. 1b. The peak values at $2\theta \approx 23.6$, 42.4, and 60° in the XRD pattern (Fig. 1c) correspond to the (002) plane of graphitic carbon,[34] (100) plane, determining the longitudinal dimensions of the structural element[35] and (103) plane of carbon in the hexagonal graphitic lattice,[36] respectively. The nature of the carbon core was further clarified by Raman spectroscopy. Both the D and G bands, which correspond to the sp^2 and sp^3 hybrid character of the carbon atoms, are visible in the Raman spectrum shown in Fig. 1d. The G band observed at 1545 cm^{-1} originates from the in-plane vibrations of sp^2 linked carbon atoms, whereas the D band at 1368 cm^{-1} suggests structural flaws in the graphite structure caused by substituted framework carbons, corresponding to out of plane C–C vibrations.[37,38] The intensity ratio (I_D/I_G) value is 0.88, demonstrating significant functionalization of the carbon framework in PD-CNDs.

The functional groups present in the PD-CNDs were identified using FT-IR spectroscopy (Fig. 1e) and XPS (Fig. 2). The broadband shown at 3427 cm^{-1} denotes –O–H and/or –N–H stretching. The bands at 2923 and 2848 cm^{-1} are designated as

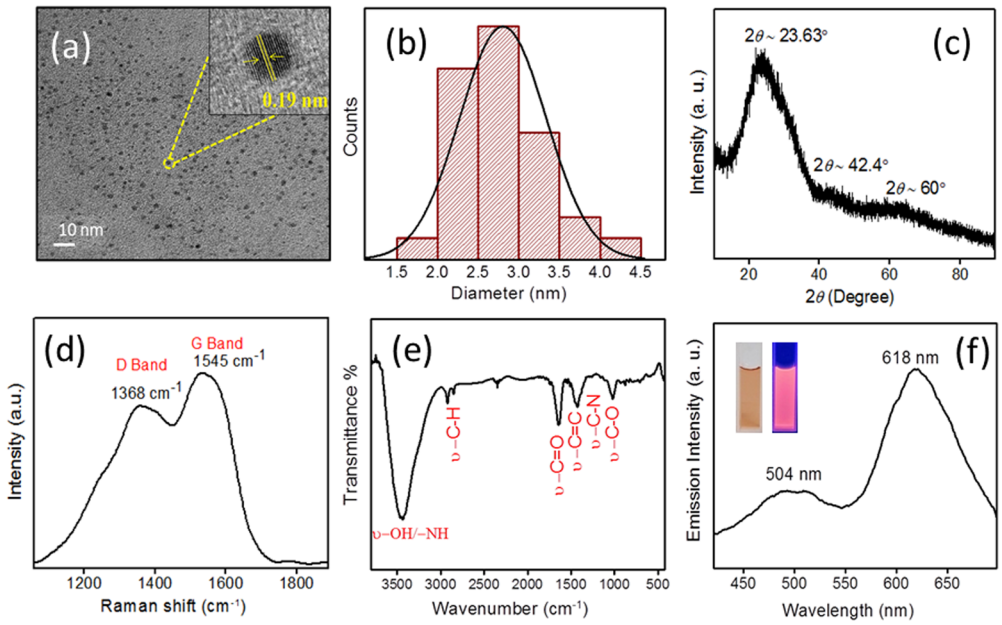

Fig. 1 (a) TEM image of PD-CNDs (inset: high resolution TEM image showing the lattice fringes with a *d*-spacing value of 0.19 nm) and (b) particle size distribution determined from the TEM image. (c) XRD profile, (d) Raman spectrum, (e) FT-IR spectrum and (f) fluorescence emission spectrum (λ_{ex}= 360 nm) of PD-CNDs (inset: image of PD-CNDs aqueous dispersion under daylight and 365 nm UV light.).

the asymmetric stretching and symmetric vibrations of –C–H. The bands produced by the –C═O/–C═N and –C–O stretching were observed at 1637 and 1021 cm^{-1}. The bands at 1510 and 1425 cm^{-1} are assigned to typical aromatic ring skeleton vibrations and the presence of –C–N moieties.[39–41] Thus, amino (–NH, $–NH_2$), carbonyl, carboxyl (–C═O/–COOH), and hydroxyl (–OH) groups are indicated as functionalities present in the core. XPS results are used to obtain more precise information in this regard (Fig. 2). Three significant peaks at 288.75, 402.51, and 534.75 eV were observed for the PD-CNDs and assigned to C 1s, N 1s, and O 1s, respectively, with corresponding atomic percentages of 71.88, 11.41, and 14.71% (Fig. 2a). The C 1s peak is further fitted in Fig. 2b to represent the moieties C–C/C═C (284.35 eV), C–N/C–O (285.31 eV), and C═N/C═O (286.36 eV).[41,42] The O 1s peak upon curve fitting shows the presence of functionalities C═O, C–O/C–OH, and O–C═O, as indicated by the peaks at 531.37, 532.47, and 533.14 eV in the respective order (Fig. 2c).[43] the N 1s spectral peak is composed of three peaks, observed at 398.39, 400.18, and 399.21 eV, respectively, signifying pyridinic, pyrrolic, and amino nitrogens (Fig. 2d).[44] Combining the information from XPS and FT-IR spectroscopy, amino, carboxyl, and hydroxyl groups are predicted as the surface functional groups on the carbon framework. An N-doped carbon core containing pyridinic and pyrrolic nitrogen is also expected.

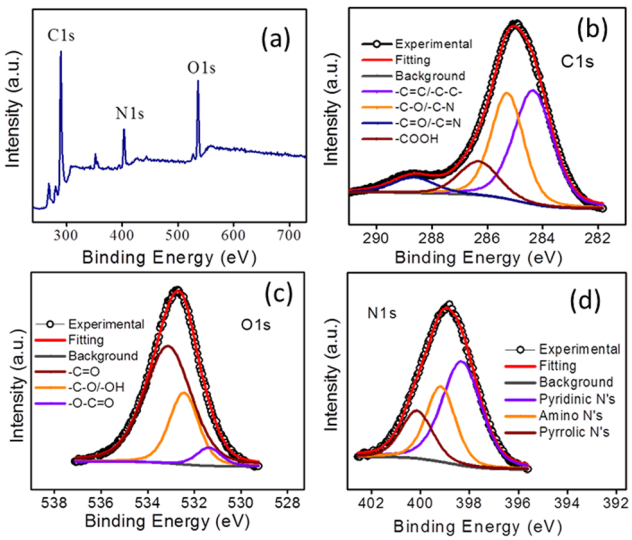

Fig. 2 (a) The XPS survey spectrum of PD-CNDs; (b)–(d) XPS fitting curves of C 1s, O 1s and N 1s of PD-CNDs.

UV-vis absorption and fluorescence spectroscopy were used to examine the optical properties of the system. The aqueous solution of PD-CNDs exhibited a brownish-red appearance in visible light and produced an orange-red colour when exposed to 365 nm UV light (Fig. 1f inset). The UV-vis absorption spectrum of the PD-CNDs illustrated in Fig. S1 (ESI†), shows prominent peaks at 278 nm in the high-energy UV region and 510 nm in the visible region. A shoulder peak was also noted at 365 nm, which accounts for the n–π* transition arising from various surface functional groups. The peak noted in the 240–280 nm region is assigned to π–π* transition, which accounts for the carbonyl, aromatic C═C double bond and –C═N groups. The peak at 510 nm was caused by extended π-conjugation in the carbon structure and explains Mie scattering.[45–47]

Fig. 1f shows the fluorescence spectrum of the PD-CNDs. The spectrum clearly shows that the system is dual-emissive, with emission maxima at 504 and 618 nm, resulting in an orange-red emission. The emission spectra of PD-CNDS obtained by exciting the samples at different wavelengths showed that the position of

the second emission peak at 618 nm was not altered, while the emission peak at 504 nm was excitation wavelength-dependent (Fig. S2, ESI†). This is usually caused by the existence of several emissive states on PD-CNDs, and it is related to the functional groups in the structure. With an increase in the excitation wavelength, the peak at the lower wavelength undergoes a red-shift and gradually disappears, and this shift is assigned to surface defect emission.[48] The photo-stability test conducted by continuous exposure of the system to UV radiation (Fig. S3, ESI†) demonstrates that the emission of these particles is noticeably steady when dispersed in water. The fluorescence lifetime decay profile of the PD-CND aqueous dispersion was monitored at 618 nm and fitted by mono-exponential decay with a decay constant of 2.40 ns (Fig. S4, ESI†).

Visual detection of Cu^{2+} ion in ppm levels

The results of the interaction of various metal ions with the PD-CND solutions are shown in Fig. 3a. It was quite interesting to observe that the PD-CND solution turned black, resulting in a black precipitate within a minute in the presence of Cu^{2+} ions, which can be easily observed by the naked-eye. As indicated in Fig. 3a, no other metal ions tested could evoke such a response when in contact with the PD-CND solution at this micromolar concentration. Fig. 3b shows the colour change of the PD-CND solution in the presence of added Cu^{2+} ions over time. The colour change of the PD-CND solution upon the addition of different concentrations of Cu^{2+} ions is shown in Fig. 3d. The lowest concentration of copper ions that could affect a visible colour change to the solution was 20 μM (Fig. S5, ESI†), a highly significant value in the context that the permissible amount of copper in drinking water is 31.5 μM (as per WHO). The visual

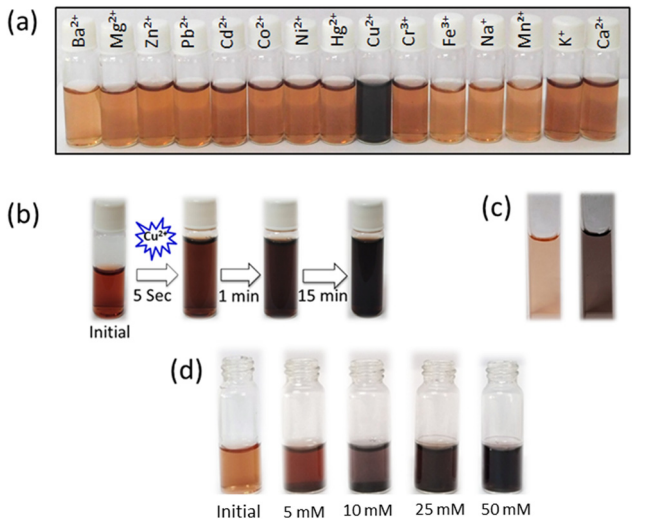

Fig. 3 (a) Visual sensing of Cu^{2+} ions using PD-CNDs showing the selective response of cupric ions (mM) towards carbon nanodots. (b) Photographs showing the response to PD-CNDs to Cu^{2+} at various time intervals. (c) PD-CND solution without and (left) and with (right) cupric ions. (d) Photographs showing the concentration dependent response of cupric ions (images captured after 30 min of Cu^{2+} ion (mM) solution addition).

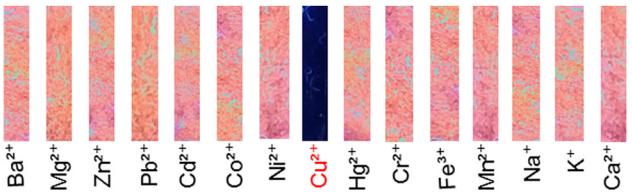

Fig. 4 Photographs of PD-CND test paper strips under 365 nm UV exposure when in contact with different metal ion solutions.

detection can be further extended to different types of water. The characteristic colour change is observed in all water samples selected for analysis. The details of the real sample analysis are provided in Fig S6 and S7 and Table S1 (ESI†). To test the interference of other ions in the visual detection of Cu^{2+} ions, a mixture of metal ions (Ba^{2+}, Mg^{2+}, Zn^{2+}, Pb^{2+}, Cd^{2+}, Co^{2+}, Ni^{2+}, Hg^{2+}, Cr^{3+}, Fe^{3+}, Na^{+}, Mn^{2+}, K^{+}, Ca^{2+}) without and with Cu^{2+} ions were introduced into the PD-CNDs solution. A mixture of metal ions without Cu^{2+} ions failed to respond through colour variation, whereas the mixture containing Cu^{2+} ions showed drastic colour change. The interference-free performance and reliability of the method were evident from the experimental results (Fig. 3c).

Fig. 4 demonstrates the naked-eye detection of Cu^{2+} using a solid-state test strip prepared by coating an ordinary filter paper with PD-CND solution, followed by drying. Orange luminescence is exhibited by the strip upon illumination with UV radiation. The strip is subsequently made in contact with metal ion solutions and dried. Intriguingly, the strip treated with copper ions appears black under UV light, indicating quenched fluorescence. The lowest concentration of cupric ions that affected this colour change was noted as 1 mM.

Quantification of Cu^{2+} ions using fluorimetry

In addition to the above-mentioned method, Cu^{2+} ion detection can be achieved at lower concentrations using PD-CNDs *via* fluorescence spectroscopy (Fig. 5). Cu^{2+} ions efficiently quench the orange-red luminescence of PD-CNDs (Fig. 5a inset). The change was observed even at lower concentrations of cupric ions. The luminescence quenching of PD-CNDs after the addition of Cu^{2+} ion solution is shown in Fig. 5a. The Stern–Volmer plot depicting the relative fluorescence quenching (F_0–F/F_0) *versus* concentration of Cu^{2+} ions shown in Fig. 5b exhibited a linear relationship. Fig. 5c shows the selectivity of PD-CNDs towards the target analyte. Notably, Cu^{2+} ions substantially quench the fluorescence of PD-CNDs, whereas a negligible effect is observed for other metal ions. To assess the selectivity of the sensor, the response of PD-CNDs towards potentially interfering ions was examined using the following metal ions; Ba^{2+}, Mg^{2+}, Zn^{2+}, Pb^{2+}, Cd^{2+}, Ni^{2+}, Hg^{2+}, Cr^{3+}, Fe^{3+}, Na^{+}, Mn^{2+}, K^{+}, and Ca^{2+} (Fig. 5d). Under the reported conditions, the experimentally determined limit of detection for Cu^{2+} ions is 2.28 μM, which is well below the permissible limit of Cu^{2+} ions in drinking water (20 μM) set by the US Environmental Protection Agency.[49] The excellent reproducibility of the results is evident from the Cu^{2+} sensing data obtained using PD-CNDs synthesised in another batch under identical experimental

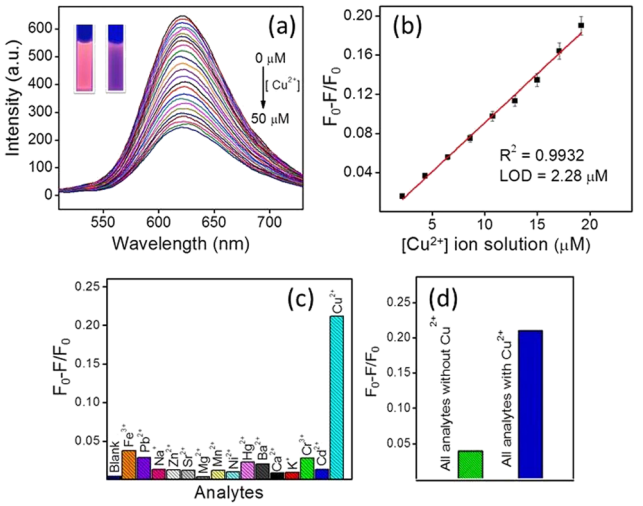

Fig. 5 (a) Fluorescence emission spectra of PD-CNDs in the presence of different concentration of Cu^{2+} ions (λ_{ex} = 440 nm). Inset shows luminescence of PD-CNDs solution in the absence and presence of Cu^{2+} ions (10 μM) under 365 nm of UV light illumination. (b) The Stern–Volmer plot for the quenching of PD-CND emission *via* successive addition of Cu^{2+} ions. (c) Selectivity of PD-CNDs towards various analyte metal ions. (d) Illustration of interference free detection of cupric ions in the presence of other metal ions.

conditions. The results related to this are presented in Fig. S11 (ESI†). The LOD value obtained at this time (2.29 μM) is in close agreement with the results of the previous experiment. Table S2 (ESI†) presents various carbon nanodot-based cupric ion sensors operating through a fluorimetric route, which are efficient in tracing this ion. This system is inferior to some of these materials in terms of LOD values. However, PD-CNDs can efficiently quantify cupric ions in drinking water, where the permissible Cu^{2+} amount is 31.5 μM.

Possible sensing mechanism

Generally, fluorescence quenching involves various interactions, including inner filter effects, non-radiative decay, electron transfer processes, and ion-binding interactions. To gain deeper insights into the quenching fluorescence, lifetime decay analysis was conducted, focusing on charge transfer and exciton recombination processes in the presence and absence of Cu^{2+} ions. Fig. S8a (ESI†) shows the fluorescence lifetime decays of PD-CNDs. Interestingly, the fluorescence lifetime (τ) remains nearly constant ($\tau_{PD\text{-}CNDs}$ = 2.40 ns, $\tau_{PD\text{-}CNDs@Cu}$ = 2.47 ns) before and after the addition of Cu^{2+} ions, indicating that the quenching mechanism involves complex formation (static quenching) rather than dynamic.[50,51] The absence of Förster resonance energy transfer (FRET) is identified by the negligible overlap between the absorption spectrum of Cu^{2+} and the emission spectrum of PD-CNDs (Fig. S8b, ESI†). Furthermore, the inner filter effects were ruled out, as evidenced by the lack of overlap between the excitation spectra of the PD-CNDs and the absorption spectra of Cu^{2+} ions (Fig. S8b, ESI†). An intriguing observation in our study is the blue shift in the π–π* transition of PD-CNDs in the presence of Cu^{2+} ions, accompanied by absorbance quenching (Fig. S8c, ESI†). The observed blue shift is attributed to the formation of the PD-CNDs@Cu complex resulting from the interaction between Cu^{2+} ions and PD-CNDs. Collectively, these findings contribute to a comprehensive understanding of quenching mechanisms that involve complex formation. The schematic representation of the luminescence reduction is given in Scheme S1 (ESI†).

Copper hydroxynitrate formation

The reason behind the visual detection of Cu^{2+} ions is suggested to be the complex formation between PD-CNDs and Cu^{2+} ions, which is supported by the various analytical results shown in Fig. 6 and 7. It is clear from the FT-IR spectrum (Fig. 6b) that additional bands corresponding to –Cu–O and $-NO_2$ vibrations are present (1600–1500 cm^{-1} and 1400–1300 cm^{-1}), indicating the complex formation between PD-CNDs and Cu^{2+} ions. The broadband shown in the range 3600–3200 cm^{-1} denotes –O–H and/or –N–H stretching. The Cu–O–H bonds present in PD-CND@Cu give rise to bending absorptions at different frequencies, depending on the degree of H bonding, which is correlated with the wideness of the band. The bands were located at 878, 784 and 672 cm^{-1}, respectively. The bands at 1451, 1385, and 1019 cm^{-1} indicate different $-ONO_2$ – stretching vibrations in PD-CND@Cu.[52,53] The Raman spectrum (Fig. 6c) had a similar correlation with the reported vibration frequencies of the signals.

The bands corresponding to Cu–O (279 and 498 cm^{-1}) Cu–ONO_2 bonds (385 cm^{-1}), and the vibrations of the nitrate groups (613 and 1010 cm^{-1}) are observed.[54–56] In addition, the D and G bands present in the PD-CNDs were retained with a small shift in PD-CNDs@Cu. TEM and field emission scanning electron microscopy (FE-SEM) analysis assign plate-like morphology for the complex formed (Fig. 7a–c). The energy-dispersive X-ray

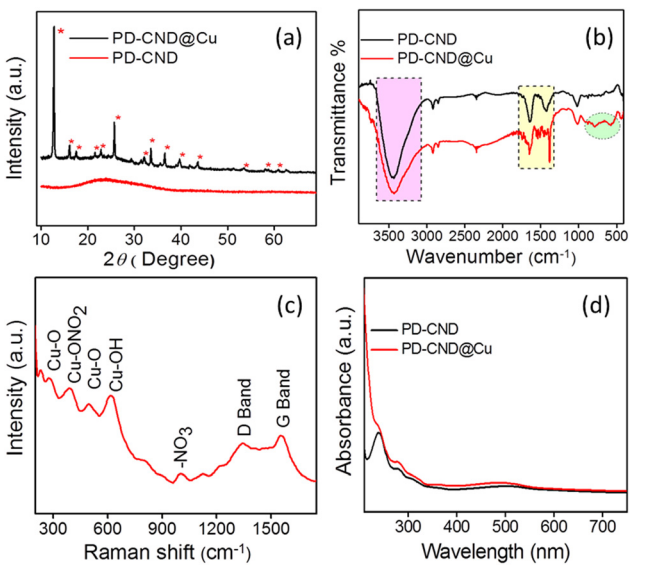

Fig. 6 (a) XRD pattern of PD-CNDs and PD-CND@Cu, (b) FT-IR spectra of PD-CNDs and PD-CNDs@Cu, (c) Raman spectrum of PD-CNDs@Cu, and (d) UV-vis absorption spectra of PD-CNDs and PD-CNDs@Cu.

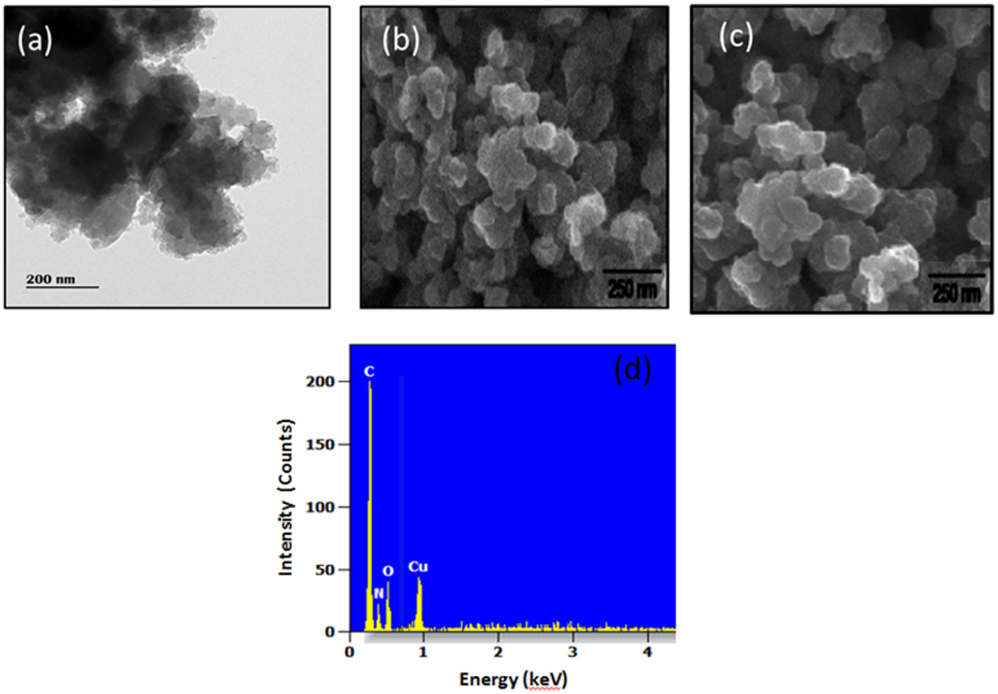

Fig. 7 (a)TEM image of PD-CNDs@Cu. (b) and (c) FE-SEM images of PD-CNDs@Cu. (d) EDAX pattern of PD-CNDs@Cu.

spectroscopy analysis (EDAX) results presented in Fig. 7d confirm the incorporation of copper in the system. This was further confirmed by elemental mapping (Fig. S9, ESI†). A comparison of the XRD pattern of PD-CND@Cu with that of PD-CNDs (Fig. 6a) reveals the presence of a broad peak centred at 2θ value 23.4°corresponds to (002) plain of graphitic carbon in PD-CNDs, and additional sharp crystalline peaks are observed at 12.73, 15.97, 17.69, 21.45, 22.81, 25.71, 29.30, 32.03, 33.56, 36.47, 39.55, 43.65, 53.56, 58.68, 60.73 and 62.61° matching with copper hydroxynitrate.[54,57]

The material, $Cu_2(OH)_3NO_3$, also known as basic Cu(II) salt, falls within the family of anionic clays, resembling double hydroxides or hydrotalcite-like materials.[58,59] They are featured by H-bonding between planar layers of $[Cu_2(OH)_3]^+$. The material has technological applications in vehicle airbags,[60] catalysts,[61,62] ion exchange,[63] superhydrophobic surface,[64] and scalable copper ink,[65] and it also serves as a precursor to $Cu(OH)_2$, CuO,[66] and nano-Cu(0).[67] Here, copper oxide nanoparticles are achieved by the calcination of PD-CNDs@Cu at 500 °C for 2 h, which is confirmed by the XRD pattern (Fig. 8). The system is also admired for its interesting magnetic properties. Many approaches have been used to synthesize $Cu_2(OH)_3NO_3$. Conventionally, special synthesis strategies (vigorous stirring, solvothermal, or ultrasonic conditions), including alkali hydroxides and assistant reagents, are used to achieve copper hydroxynitrate from copper salts, including plasma electrolysis,[68] solution immersion[64] and urea hydrolysis.[52] In this scenario, the synthesis of copper hydroxynitrate *via* the route presented in this study offers an effortless pathway that involves a simple mixing process. Hence a dual purpose is served by the N-doped CNDs during interaction with cupric ions.

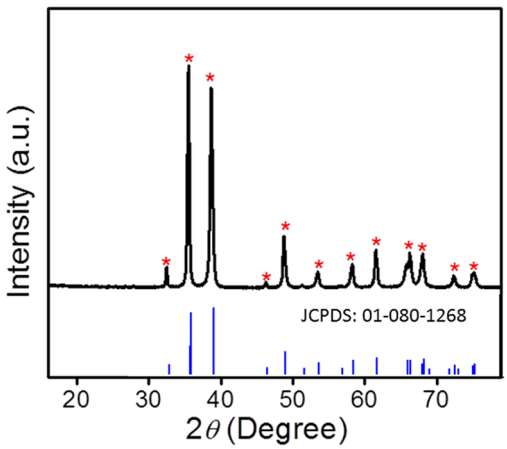

Fig. 8 XRD pattern of CuO synthesized from PD-CND@Cu.

Conclusions

In summary, this study presents fluorescent N-doped carbon nanodots (PD-CNDs) synthesized from *p*-phenylenediamine for the rapid visual detection and quantification of Cu(II) ions in drinking water. The comprehensive characterization of PD-CNDs revealed an N-doped carbon core anchored with carboxyl, amino, hydroxyl, and carbonyl functional groups. Stable orange-red fluorescence is displayed by the system. The visual detection of Cu^{2+} ions was enabled by an instantaneous colour change in both the aqueous dispersion of the particles and the paper sensor strips. Interference-free selectivity was demonstrated for Cu^{2+} ions in both cases. The static quenching process through complex formation between PD-CNDs and

Cu^{2+} ions is operative in this process. The quantification of Cu^{2+} ions using fluorimetry provides a limit of detection of 2.28 μM. An in-depth analysis using XRD, EDS, FT-IR, and Raman spectroscopy suggested the formation of copper hydroxynitrate as the basis of this detection strategy. This study demonstrated the usefulness of PD-CNDs as a promising platform for the selective visual detection of Cu^{2+} ions, which are generally useful for environmental monitoring and water quality assessment.

Data availability

Data will be made available from the authors upon request.

Conflicts of interest

There are no conflicts to declare.

Acknowledgements

N. V. acknowledges the University of Calicut for the financial support. The authors are grateful to CIF, University of Calicut, for providing the analytical facilities. Financial assistance received from DST under the FIST program is also acknowledged.

References

1 K. J. Barnham, C. L. Masters and A. I. Bush, *Nat. Rev. Drug Discovery*, 2004, **3**, 205–214.
2 J. H. Viles, *Coord. Chem. Rev.*, 2012, **256**, 2271–2284.
3 E. Madsen and J. D. Gitlin, *Annu. Rev. Neurosci.*, 2007, **30**, 317–337.
4 J. C. Lee, H. B. Gray and J. R. Winkler, *J. Am. Chem. Soc.*, 2008, **130**, 6898–6899.
5 Y. H. Hung, A. I. Bush and R. A. Cherny, *J. Biol. Inorg. Chem.*, 2010, **15**, 61–76.
6 C. Vulpe, B. Levinson, S. Whitney, S. Packman and J. Gitschier, *Nat. Genet.*, 1993, **3**, 7–13.
7 K. Jomova, M. Makova, S. Y. Alomar, S. H. Alwasel, E. Nepovimova, K. Kuca, C. J. Rhodes and M. Valko, *Chem.-Biol. Interact.*, 2022, 110173.
8 Y. Zhu, K. Inagaki and K. Chiba, *J. Anal. At. Spectrom.*, 2009, **24**, 1179–1183.
9 S. Ashoka, B. M. Peake, G. Bremner, K. J. Hageman and M. R. Reid, *Anal. Chim. Acta*, 2009, **653**, 191–199.
10 D. Chen, B. Hu and C. Huang, *Talanta*, 2009, **78**, 491–497.
11 O. Acar, *Talanta*, 2005, **65**, 672–677.
12 D. Cotton and D. Jenkins, *Spectrochim. Acta, Part B*, 1970, **25**, 283–288.
13 M.-S. Chan and S.-D. Huang, *Talanta*, 2000, **51**, 373–380.
14 R. Sahu, S. Yadav, K. C. Gunturu and A. R. Kapdi, *J. Org. Chem.*, 2023, **88**, 15118–15129.
15 A. Helal, M. Naeem, M. Fettouhi and M. H. Zahir, *Molecules*, 2021, **26**, 5773.
16 A. Helal, M. N. Shaikh and M. A. Aziz, *J. Photochem. Photobiol., A*, 2020, **389**, 112238.
17 T. Chopra, S. Sasan, L. Devi, R. Parkesh and K. K. Kapoor, *Coord. Chem. Rev.*, 2022, **470**, 214704.
18 K. M. Trevino, C. R. Wagner, E. K. Tamura, J. Garcia and A. Y. Louie, *Dyes Pigm.*, 2023, **214**, 110881.
19 H. Song, M. Huo, M. Zhou, H. Chang, J. Li, Q. Zhang, Y. Fang, H. Wang and D. Zhang, *Crit. Rev. Anal. Chem.*, 2024, **54**, 1987–2006.
20 A. Tamborelli, M. López Mujica, G. Servetti, D. Venegas-Yazigi, P. Hermosilla-Ibáñez, P. Dalmasso and G. Rivas, *Chemosensors*, 2025, **13**, 35.
21 Y. Lu, G. Yu, X. Wei, C. Zhan, J.-W. Jeon, X. Wang, C. Jeffryes, Z. Guo, S. Wei and E. K. Wujcik, *Adv. Compos. Hybrid Mater.*, 2019, **2**, 711–719.
22 F. S. Awad, K. M. AbouZied, A. M. Bakry, W. M. Abou El-Maaty, A. M. El-Wakil and M. S. El-Shall, *Anal. Chim. Acta*, 2020, **1140**, 111–121.
23 S. Mohapatra, S. Sahu, N. Sinha and S. K. Bhutia, *Analyst*, 2015, **140**, 1221–1228.
24 S. S. Wee, Y. H. Ng and S. M. Ng, *Talanta*, 2013, **116**, 71–76.
25 Y. Guo, Z. Wang, H. Shao and X. Jiang, *Analyst*, 2012, **137**, 301–304.
26 Y. Guo, Z. Wang, H. Shao and X. Jiang, *Carbon*, 2013, **52**, 583–589.
27 S. N. A. Mohd Yazid, S. F. Chin, S. C. Pang and S. M. Ng, *Microchim. Acta*, 2013, **180**, 137–143.
28 H. Wang, W. Mu, S. Wang, L. Shi, T. Ma and Y. Lu, *Spectrochim. Acta, Part A*, 2024, **305**, 123460.
29 P. Das, S. Ganguly, M. Bose, S. Mondal, A. K. Das, S. Banerjee and N. C. Das, *Mater. Sci. Eng., C*, 2017, **75**, 1456–1464.
30 Y. Liu, Y. Zhao and Y. Zhang, *Sens. Actuators, B*, 2014, **196**, 647–652.
31 G. Huang, X. Luo, W. Lin, W. Tang, T. Yue, J. Wang and Z. Li, *Dyes Pigm.*, 2022, **203**, 110381.
32 R. Bisauriya, S. Antonaroli, M. Ardini, F. Angelucci, A. Ricci and R. Pizzoferrato, *Sensors*, 2022, **22**, 2487.
33 A. Beiraghi and S. A. Najibi-Gehraz, *Sens. Actuators, B*, 2017, **253**, 342–351.
34 V. Raveendran and R. N. Kizhakayil, *ACS Omega*, 2021, **6**, 23475–23484.
35 A. Popova, *Coke Chem.*, 2017, **60**, 361–365.
36 Z. Li, C. Lu, Z. Xia, Y. Zhou and Z. Luo, *Carbon*, 2007, **45**, 1686–1695.
37 V. Ramanan, S. K. Thiyagarajan, K. Raji, R. Suresh, R. Sekar and P. Ramamurthy, *ACS Sustainable Chem. Eng.*, 2016, **4**, 4724–4731.
38 S. Kalytchuk, L. Zdražil, M. Scheibe and R. Zbořil, *Nanoscale*, 2020, **12**, 8379–8384.
39 Y. An, X. Lin, Y. Zhou, Y. Li, Y. Zheng, C. Wu, K. Xu, X. Chai and C. Liu, *RSC Adv.*, 2021, **11**, 26915–26919.
40 M. Vedamalai, A. P. Periasamy, C.-W. Wang, Y.-T. Tseng, L.-C. Ho, C.-C. Shih and H.-T. Chang, *Nanoscale*, 2014, **6**, 13119–13125.
41 H. Liu, J. Yang, Z. Li, L. Xiao, A. A. Aryee, Y. Sun, R. Yang, H. Meng, L. Qu and Y. Lin, *Anal. Chem.*, 2019, **91**, 9259–9265.
42 J. Bai, Y. Ma, G. Yuan, X. Chen, J. Mei, L. Zhang and L. Ren, *J. Mater. Chem. C*, 2019, **7**, 9709–9718.

43 J. Bai, G. Yuan, Y. Zhu, Z. Huang, L. Zhang, X. Wang, S. Wu and L. Ren, *J. Phys. Chem. C*, 2021, **125**, 18543–18551.
44 J. Wang, J. Wang, W. Xiao, Z. Geng, D. Tan, L. Wei, J. Li, L. Xue, X. Wang and J. Zhu, *Anal. Methods*, 2020, **12**, 3218–3224.
45 L. Han, S. G. Liu, J. X. Dong, J. Y. Liang, L. J. Li, N. B. Li and H. Q. Luo, *J. Mater. Chem. C*, 2017, **5**, 10785–10793.
46 H. Ding, S.-B. Yu, J.-S. Wei and H.-M. Xiong, *ACS Nano*, 2016, **10**, 484–491.
47 S. Qu, X. Wang, Q. Lu, X. Liu and L. Wang, *Angew. Chem., Int. Ed.*, 2012, **51**, 12215–12218.
48 T. Zhang, J. Zhu, Y. Zhai, H. Wang, X. Bai, B. Dong, H. Wang and H. Song, *Nanoscale*, 2017, **9**, 13042–13051.
49 J. Liu and Y. Lu, *J. Am. Chem. Soc.*, 2007, **129**, 9838–9839.
50 F. Zu, F. Yan, Z. Bai, J. Xu, Y. Wang, Y. Huang and X. Zhou, *Microchim. Acta*, 2017, **184**, 1899–1914.
51 F. Noun, E. A. Jury and R. Naccache, *Sensors*, 2021, **21**, 1391.
52 C. Henrist, K. Traina, C. Hubert, G. Toussaint, A. Rulmont and R. Cloots, *J. Cryst. Growth.*, 2003, **254**, 176–187.
53 E. K. Güner and A. K. Özer, *J. Turk. Chem. Soc., Sect. B*, 2017, **1**, 183–192.
54 D. C. Pereira, D. L. A. d Faria and V. R. Constantino, *J. Braz. Chem. Soc.*, 2006, **17**, 1651–1657.
55 D. Videira-Quintela, F. Guillen, G. Montalvo and O. Martin, *Colloids Surf., B*, 2020, **195**, 111216.
56 X. Santos, J. Rodríguez, F. Guillén, J. Pozuelo, J. Molina-Guijarro, D. Videira-Quintela and O. Martín, *Polymers*, 2023, **15**, 1661.
57 X. Zheng, K. Wu, J. Mao, X. Jiang, L. Shao, X. Lin, P. Li, M. Shui and J. Shu, *Electrochim. Acta*, 2014, **147**, 765–772.
58 M. Meyn, K. Beneke and G. Lagaly, *Inorg. Chem.*, 1993, **32**, 1209–1215.
59 S. P. Newman and W. Jones, *J. Solid State Chem.*, 1999, **148**, 26–40.
60 H. Schmid and N. Eisenreich, *PEP*, 2000, **25**, 230–235.
61 T. Dai and Y. Mao, *Chem. Phys. Lett.*, 2020, **739**, 137018.
62 S. Wang, X. Zhang, L. Pan, F.-M. Zhao, J.-J. Zou, T. Zhang and L. Wang, *Appl. Catal., B*, 2015, **164**, 234–240.
63 B. Liu, *Nanoscale*, 2012, **4**, 7194–7198.
64 L. Kong, X. Chen, G. Yang, L. Yu and P. Zhang, *Appl. Surf. Sci.*, 2008, **254**, 7255–7258.
65 G. L. Draper, R. Dharmadasa, M. E. Staats, B. W. Lavery and T. Druffel, *ACS Appl. Mater. Interfaces*, 2015, **7**, 16478–16485.
66 S. Padhi, S. Gottapu and M. G. Krishna, *Nanoscale*, 2016, **8**, 11194–11201.
67 S. Bai, S. Zhang, W. Zhou, D. Ma, Y. Ma, P. Joshi and A. Hu, *Nanomicro Lett*, 2017, **9**, 1–13.
68 M. Rezvani Jalal, H. Hojjati, J. Rezvani Jalal, S. Ebrahimi and M. R. Zangene Bighashi, *J. Interfaces Thin Films Low Dimens. Syst.*, 2019, **2**, 109–112.